ACES Asian Chemical Editorial Society

DOI: 10.1002/asia.201900751

CHEMISTRY
AN ASIAN JOURNAL
Minireview

Recent Advances in Aerosol-Assisted Spray Processes for the Design and Fabrication of Nanostructured Metal Chalcogenides for Sodium-Ion Batteries

Jin Koo Kim[+,a] Sun Young Jeong[+,b] Sae Hoon Lim,[a] Jang Hyeok Oh,[b] Seung-Keun Park,*[c] Jung Sang Cho,*[b] and Yun Chan Kang*[a]

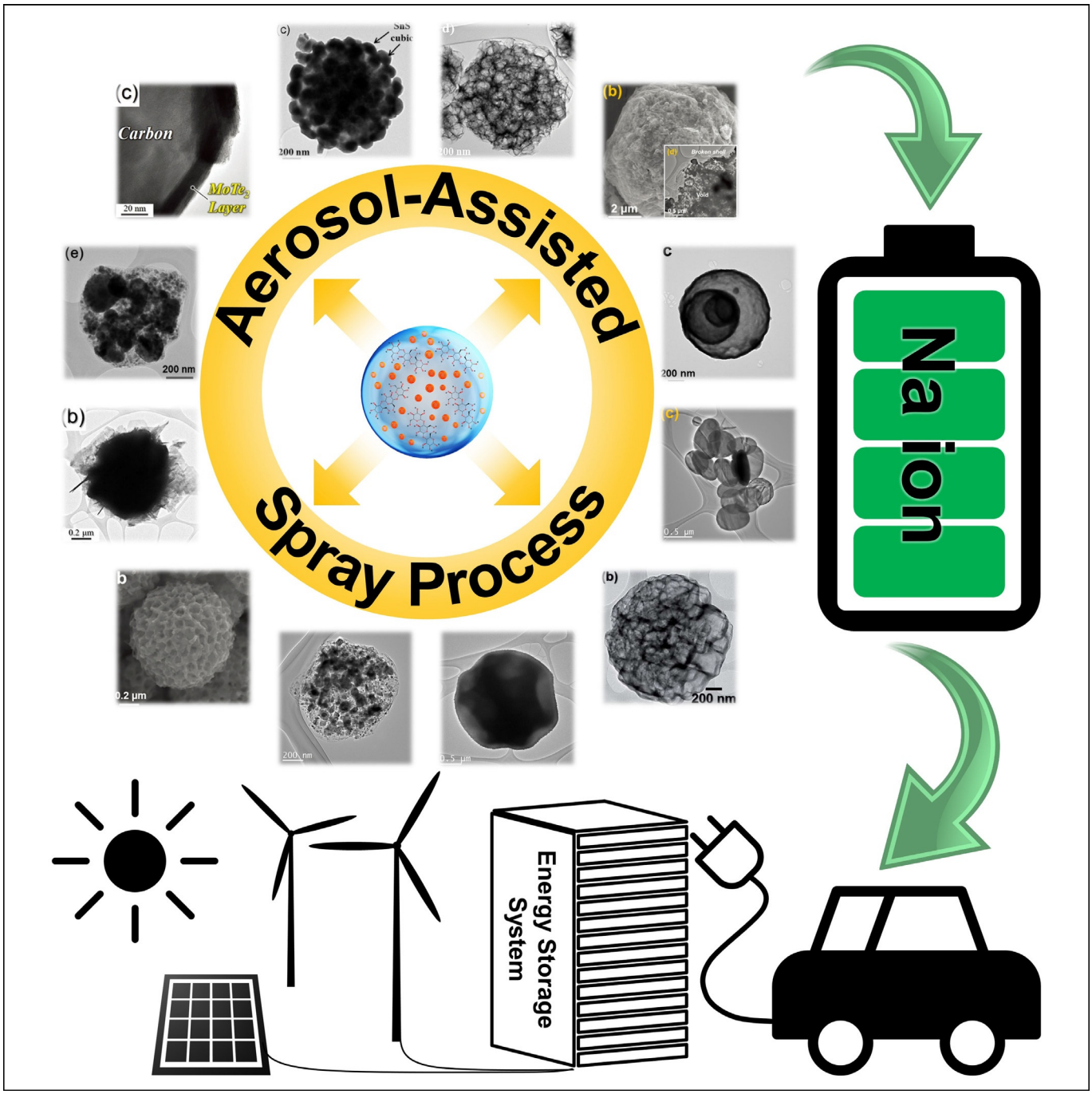

Abstract: Increasing demand for sodium-ion batteries (SIBs), one of the most feasible alternatives to lithium ion batteries (LIBs), has resulted because of their high energy density, low cost, and excellent cycling stability. Consequently, the design and fabrication of suitable electrode materials that govern the overall performance of SIBs are important. Aerosol-assisted spray processes have gained recent prominence as feasible, scalable, and cost-effective methods for preparing electrode materials. Herein, recent advances in aerosol-assisted spray processes for the fabrication of nanostructured metal chalcogenides (e.g., metal sulfides, selenides, and tellurides) for SIBs, with a focus on improving the electrochemical performance of metal chalcogenides, are summarized. Finally, the improvements, limitations, and direction of future research into aerosol-assisted spray processes for the fabrication of various electrode materials are presented.

1. Introduction

There is an ever-increasing demand for sustainable energy sources and reliable energy-storage devices to replace traditional fossil fuels, which have raised serious environmental concerns.[1–3] Rechargeable batteries, one of the most successful energy-storage devices, reversibly stores electrical energy in the form of chemical energy in the electrodes by repeated charge–discharge processes. The commercialization of lithium ion batteries (LIBs) has revolutionized every aspect of our lifestyle; LIBs are currently the most extensively used power source for various applications, such as portable electronics and electric vehicles.[4–6]

Unfortunately, however, lithium sources are scarce and unevenly distributed, such that they may not be sufficient to meet surging global demand.[7–9] In response to this concern, sodium-ion batteries (SIBs) have been spotlighted recently as a viable alternative to LIBs because sodium is cheap, virtually inexhaustible, and has similar physicochemical properties to lithium.[9–11] Accordingly, the development of suitable electrode materials, which govern the overall performance of SIBs, has attracted research interest. Significant progress has been achieved in the synthesis of cathode materials for SIBs by adapting the accumulated knowledge of LIB technologies, but the development of SIB anode materials is challenging and far from satisfactory, mainly because of the larger ionic radius of Na^+ (1.02 Å) compared with Li^+ (0.76 Å) and the slower diffusion kinetics of Na^+.[11–13] Thus, it is of significant interest to develop appropriate anode materials for SIBs in the near future.

The reaction mechanisms of the anode materials of SIBs are basically analogous to those of LIBs, and can be categorized as 1) intercalation, 2) alloying, and 3) conversion reactions.[14–17] Materials that undergo intercalation reactions feature stable cycling performance and a low working potential, but have low theoretical capacity.[18–20] Alloying-type materials, such as P, Ge, Sn, and Sb, form Na-rich alloys during the electrochemical reactions and exhibit high theoretical capacity with a low working potential.[21,22] Conversion-type materials have attracted significant attention because of their higher Na^+ storage capability compared with intercalation-type materials.[23,24] The general conversion reaction can be written as $M_aX_b + (bc)\,Na \rightleftarrows a\,M + b\,Na_cX$, in which M is a transition metal and X is a nonmetal. Full reduction of MX to form M during the sodiation process leads to a higher capacity.[23] Recently, metal chalcogenide materials, in particular sulfides and selenides, have attracted increasing attention as promising anode materials for SIBs.[24–32] Metal chalcogenides have increased bond lengths and correspondingly weaker binding energy, which reduces the energy consumption of the sodiation/desodiation reaction.[23–26] Furthermore, their discharge products (Na_2S and Na_2Se for sulfides and selenides, respectively) afford better Na^+ conductivity and lower formation enthalpies than Na_2O.[24–26] Although metal chalcogenides suffer from low initial Coulombic efficiency and irreversible capacity loss, they exhibit higher reversible capacity with improved stability and a superior rate performance compared with their oxide counterparts. However, to improve their electrochemical properties further, morphological and compositional optimizations should be taken into consideration in a way that offers a high active surface area, a reduced Na^+ diffusion length, good mechanical stability, and facile electron transport pathways during the electrochemical reaction.[33] The most commonly adapted strategies for optimization are 1) introduction of nanostructured design, 2) composition control, and 3) hybridization with other materials (typically carbon).[33–37] These strategies are often combined to maximize the overall performance of the electrode materials. Thus, many research groups have put tremendous effort into the synthesis of various nanostructured electrode materials, such as core–shell,[38] porous,[39] hierarchical,[40] hollow,[41] and yolk–shell[42] structures, along with carbon modification. These structures provide more contact area between the electrode materials and the electrolyte and better structural stabili-

[a] J. K. Kim,[+] S. H. Lim, Prof. Y. C. Kang
Department of Materials Science and Engineering
Korea University
Anam-dong, Seongbuk-gu, Seoul 136-713 (Republic of Korea)
E-mail: yckang@korea.ac.kr

[b] S. Y. Jeong,[+] J. H. Oh, Prof. J. S. Cho
Department of Engineering Chemistry
Chungbuk National University
Chungdae-ro 1, Seowon-gu, Cheongju, Chungbuk 361-763 (Republic of Korea)
E-mail: jscho@cbnu.ac.kr

[c] Prof. S.-K. Park
Department of Chemical Engineering
Kongju National University
Budae-dong 275, Cheonan, Chungnam 314-701 (Republic of Korea)
E-mail: skpark09@kongju.ac.kr

[+] These authors contributed equally to this work.

The ORCID identification number(s) for the author(s) of this article can be found under:
https://doi.org/10.1002/asia.201900751.

ty, and exhibit greatly enhanced electrochemical performance compared with the bulk materials.[33–42]

Over the past few years, numerous synthetic methods have been proposed to construct a wide variety of nanostructured metal chalcogenides for SIB anodes. The chemical composition, crystallinity, and morphology of metal chalcogenide materials are closely dependent on the synthetic process. Therefore, process optimization is vital for the preparation of anode materials for high-performance SIBs. In this regard, aerosol-assisted processes, in particular spray pyrolysis and spray drying, have gained recent prominence owing to their feasibility, scalability, cost-efficiency, and minimal waste production.[43–56] Above all, these processes usually result in various nanostructured composites of nanocrystalline host materials with carbon frameworks that can effectively benefit electrochemical performance.[47–49,57]

Herein, we present recent advances in the syntheses of nanostructured metal chalcogenides by spray pyrolysis and spray drying for use as SIB anode materials. Various metal sulfide- and selenide-based anode materials will be introduced, with concise descriptions of their synthetic mechanisms and electrochemical properties. We will then review metal telluride-based anode materials, albeit briefly because of insufficient literature about them compared with sulfides and selenides. The

Jang Hyeok Oh *is a Master's degree candidate at Chungbuk National University under the supervision of Prof. Jung Sang Cho. He received his Bachelor's degree from the Department of Engineering Chemistry, Chungbuk National University, Cheongju, Korea, in 2018. His current research focuses on the synthesis of nanostructured materials for energy storage.*

Jin Koo Kim *is a Ph.D. candidate at Korea University under the supervision of Prof. Yun Chan Kang. He received his Bachelor's degree from the Department of Materials Science and Engineering, Korea University, Seoul, Korea, in 2016. His current research focuses on the development of nanostructured materials by spray processes for use in energy storage, catalysts, and gas sensors.*

Seung-Keun Park *received his Ph.D. from the Graduate School of Convergence Science and Technology, Seoul National University, Korea, in 2016. He then joined Prof. Yun Chan Kang's lab as a post-doc at the Department of Materials Science and Engineering, Korea University, Seoul, Korea. Since 2018, he has been a professor at the Department of Chemical Engineering, Kongju National University, Cheonan, Korea. His research group focuses on the design and synthesis of nanostructured materials for energy-storage applications. For details, please visit the lab website: https://agape0909.wixsite.com/gemlab.*

Sun Young Jeong *is a Master's degree candidate at Chungbuk National University under the supervision of Prof. Jung Sang Cho. He received his Bachelor's degree from the Department of Engineering Chemistry, Chungbuk National University, Cheongju, Korea, in 2018. His current research focuses on the synthesis of nanostructured materials for the energy storage.*

Jung Sang Cho *received his Ph.D. from the Interdisciplinary Program for Bioengineering, Seoul National University, Korea, in 2013, and had post-doc experience at the Department of Materials Science and Engineering, Korea University, Korea (2014–2016). Since 2016, he has been a professor at the Department of Engineering Chemistry, Chungbuk National University, Cheongju, Korea. His research group works on the development of nanostructured materials for energy storage, sensors, catalysts, displays, and biomaterials. For details, please visit the lab website: https://jjj777.wixsite.com/professor-cho.*

Sae Hoon Lim *is a Ph.D. candidate at Korea University under the supervision of Prof. Yun Chan Kang. He received his Bachelor's degree from the Department of Advanced Materials Engineering for Information & Electronics, Kyung Hee University, Suwon, Korea, in 2018. His current research focuses on the development of nanostructured materials by spray processes for use in energy storage, catalysts, and gas sensors.*

Yun Chan Kang *received his Ph.D. from the Department of Chemical Engineering, KAIST, Korea, in 1997, and had post-doc experience at the Department of Chemical Engineering, Hiroshima University in Japan (1997–1998). He became a professor at the Department of Chemical Engineering, Konkuk University, Seoul, Korea (2004–2014). Since 2014, he has been a professor at the Department of Materials Science and Engineering, Korea University, Seoul, Korea. His research group works on the development of nanostructured materials for energy storage by aerosol processes. For details, please visit the lab website: http://spray.korea.ac.kr.*

Table 1. The electrochemical performances of various metal chalcogenides synthesized by spray processes.

Sample	Voltage window [V vs. Na^+/Na]	Synthesis method	Cycle performance[a]	Rate performance[b]	Ref.
Metal sulfides					
Co_9S_8-carbon composite powder	0.001–3.0	spray pyrolysis	404/50th/0.5	326/1.5	[68]
cubic-like SnS-C composite microspheres	0.001–3.0	spray pyrolysis	433/50th/0.5	280/5.0	[69]
mesoporous MoS_2/C microspheres	0.05–3.0	spray pyrolysis	390/2500th/1.0	244/20.0	[70]
ultrasmall SnS nanoparticles embedded in carbon spheres	0.01–2.9	spray pyrolysis	518/200th/1.0	315/5.0	[71]
3D MoS_2-graphene microspheres	0.001–3.0	spray pyrolysis	323/600th/1.5	234/10.0	[72]
MoS_2-graphene hierarchical microspheres	0.01–3.0	spray drying and heat treatment	300/500th/1.0	230/5.0	[73]
WS_2-3D rGO microspheres	0.001–3.0	spray pyrolysis and heat treatment	334/200th/0.2	287/0.9	[74]
FeS-rGO composite powder	0.001–3.0	spray pyrolysis and heat treatment	547/50th/0.5	340/6.0	[75]
NiS_x hollow nanospheres/rGO composite powder	0.001–3.0	spray drying and two-step heat treatments	363/150th/0.3	377/3.0	[76]
yolk–shell structured $(Fe_{0.5}Ni_{0.5})_9S_8$ microspheres	0.01–3.0	spray pyrolysis and heat treatment	527/100th/1.0	465/5.0	[77]
multiroom-structured cobalt sulfide/carbon hybrid microspheres	0.001–3.0	spray pyrolysis and heat treatment	334/100th/0.2	411/1.0	[78]
multiroom-structured MoS_2-Ni_9S_8 microspheres	0.001–3.0	spray drying and heat treatment	459/80th/0.5	428/3.0	[79]
MoS_2/C microspheres with cubic nanorooms	0.01–3.0	spray pyrolysis, washing and heat treatment	385/350th/0.5	287/7.0	[80]
Metal selenides					
$CoSe_x$-rGO composite powder	0.001–3.0	spray pyrolysis	420/50th/0.3	357/1.0	[81]
SnSe nanoplates	0.001–3.0	spray pyrolysis	558/50th/0.3	221/2.0	[82]
$FeSe_2$-amorphous carbon composite powder	0.001–3.0	spray drying and heat treatment	379/150th/0.5	286/5.0	[83]
hierarchical $MoSe_2$ yolk–shell microspheres	0.001–3.0	spray pyrolysis and heat treatment	433/50th/0.2	345/1.5	[84]
cobalt selenide hollow microspheres	0.001–3.0	spray pyrolysis and heat treatment	467/40th/0.5	446/0.9	[85]
fullerene-like $MoSe_2$ nanoparticle-embedded CNT balls	0.001–3.0	spray pyrolysis and heat treatment	296/250th/1.0	255/5.0	[86]
mesoporous WSe_2-rGO hybrid powder	0.001–3.0	spray pyrolysis and heat treatment	238/100th/0.5	165/5.0	[87]
$MoSe_2$-rGO-CNT composite microspheres	0.001–3.0	spray pyrolysis and heat treatment	335/400th/1.0	173/30.0	[88]
$CoSe_2$@NC-NR/CNT microspheres	0.001–3.0	spray pyrolysis, coprecipitation, and selenization	484/100th/5.0	517/5.0	[89]
$CoSe_2$-$MoSe_2$-C microspheres with vacant nanorooms	0.001–3.0	spray pyrolysis and heat treatment	399/100th/0.2	317/5.0	[90]
interconnected multicavities within hollow $FeSe_2$/graphitic carbon microspheres	0.001–3.0	spray pyrolysis, washing, and two-step heat treatments	510/200th/0.2	417/5.0	[91]
multiroom structured $CoSe_2$-C microspheres	0.001–3.0	spray pyrolysis and heat treatment	393/100th/0.2	451/1.0	[78]
$MoSe_2$-NiSe-C microspheres with empty nanovoids	0.001–3.0	spray drying and heat treatment	386/80th/0.5	301/3.0	[79]
Metal tellurides					
$FeTe_2$-rGO hybrid powders	0.01–3.0	spray pyrolysis and heat treatment	293/80th/0.2	257/3.0	[95]
C@$MoTe_2$ core–shell microspheres	0.001–3.0	spray pyrolysis and heat treatment	286/200th/1.0	209/5.0	[100]

[a] These data are arranged in the order discharge capacity/cycle number/current density. The units of discharge capacity and current density are $mA\,h\,g^{-1}$ and $A\,g^{-1}$, respectively. [b] These data are arranged in the order discharge capacity/highest current density.

electrochemical properties of the metal chalcogenides discussed herein are summarized in Table 1. Finally, a summary of the current status, with new directions and prospects for the future exploration of materials synthesis using aerosol sprays, is discussed.

2. Synthesis of metal chalcogenide materials by aerosol-assisted processes

A schematic diagram of the spray pyrolysis process is illustrated in Figure 1a. The process starts with the atomization of the precursor solution into a mist. Atomization can be achieved either ultrasonically or pneumatically. Because two different fluid streams (the precursor solution and gas) are involved in pneumatic atomization, it is also called two-fluid atomization. The carrier gas then conveys the droplets to a heated reactor at a controlled flow rate. The solvent in the droplet rapidly vaporizes and the dried product (solute) undergoes one or sever-

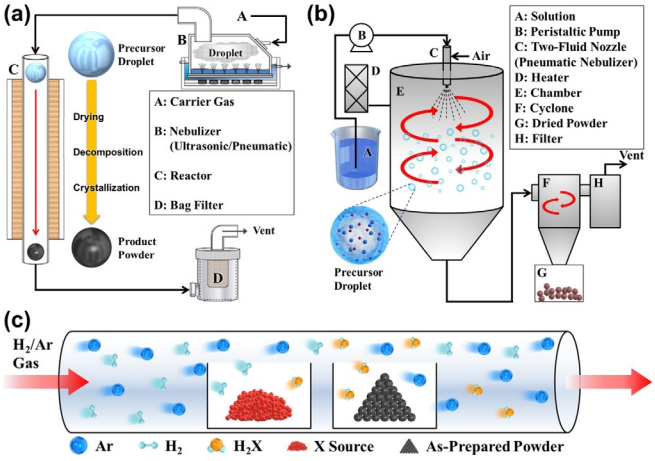

Figure 1. Schematic diagrams of a) spray pyrolysis, b) spray drying, and c) post-treatment of as-prepared powders for metal chalcogenide material syntheses.

al of the following physical and chemical processes, depending on the synthesis condition: precipitation, decomposition, crystallization, diffusion, reaction, melting, and sintering. Finally, the product powder is collected at the outlet by using a bag filter. The physical and chemical feature of the products can be easily tuned by adjusting the process parameters (i.e. temperature, type of carrier gas, flow rate, and precursor solution composition). Subsequent post-treatment of the powder is often carried out to obtain a certain morphology or phase. Because each droplet acts as an individual reactor with exactly the same composition as the precursor solution, spray pyrolysis ensures the homogeneity of the product. In addition, precise control of the composition is straightforward; thus, particles that are difficult to synthesize by conventional methods can be easily prepared by aerosol-assisted processes, as long as a precursor solution can be made.

Spray drying is a simple, facile, and scalable process that is widely adopted in the food and pharmaceutical industries. As its name indicates, it only involves the drying of precursor-containing droplets into spherical form. Recently, spray drying has emerged as one of the most promising techniques to prepare nanostructured materials. A schematic diagram of the spray drying process is shown in Figure 1b. The precursor solution is atomized by a hot-air stream at the tip of a two-fluid nozzle and sprayed downward toward the chamber. The solvent vaporizes and the solute precipitates in spherical form. The dried powder is then collected by using a cyclone separator. The size and morphology of the spray-dried particle is affected by the composition of the precursor solution, the solvent type, the inlet temperature, the feed rate, and the droplet retention time. Because the spray-dried powder is a dried form of the precursor, post-treatment of the product must be conducted before practical use.

The synthesis of metal chalcogenide materials by using aerosol-assisted processes is achieved by a reaction between the host metal/metal oxide and gaseous compounds that contain chalcogen anions at a certain temperature. One method is to dissolve the anion source in the precursor solution. Thiourea (for S) and selenium oxide (for Se) are frequently used. The use of a Te source has not been reported to date. In spray pyrolysis under an Ar/H_2 atmosphere, the anion precursors decompose into reactive H_2S and H_2Se gases, which undergo an in situ reaction with the host material particles as they pass through the reactor. In spray drying, the anion precursors in the spray-dried powder decompose during post-treatment and undergo the same process. The other method is to post-treat the as-prepared powder with the anion source precursors in a tube furnace. This process is depicted in Figure 1c, in which the inner alumina boat contains the as-prepared powder and the outer boat contains the anion precursors.

At a certain elevated temperature under an Ar/H_2 atmosphere, the anion precursors react with H_2 to generate H_2S, H_2Se, and H_2Te gases and react with the as-prepared powder to produce sulfide, selenide, and telluride materials. The reaction usually takes place for a few hours; thus, the products tend to hold their stoichiometric composition with high crystallinity.

2.1. Metal sulfides

Many different methods have been introduced to synthesize metal sulfides for use as SIB anode materials. For example, the microwave irradiation method, which can heat the reactants to a high temperature in a very short time, resulting in close contact between the components, has been successfully employed to synthesize Mo, Zn, and Ni sulfide-based anode materials for SIBs.[58–60] Electrospinning, which is a facile and versatile method to fabricate continuous nanofibers, was used to synthesize mesoporous metal sulfide/carbon nanofibers.[61–63] Hydrothermal or solvothermal methods have also been used to prepare metal sulfide materials with controlled morphologies.[64–67] However, the physicochemical properties of the materials synthesized by using conventional methods are strongly affected by the choice of metal salts and additives, which requires optimization for each material. In contrast, aerosol-assisted spray processes are a versatile technique to synthesize nonagglomerated nanostructured materials with precise composition, reproducibility, homogeneity, and high purity. Over the past few years, the aerosol-assisted synthesis of metal sulfide materials has been widely reported and it had already been proven to be a successful and scalable method for the preparation of metal oxide/carbon composite materials with controlled compositions and morphologies. Metal sulfide/carbon composites could be produced by dissolving a sulfur source in the spray solution. For example, Ko and co-worker synthesized a Co_9S_8-carbon composite by one-pot spray pyrolysis under a 10% H_2/Ar atmosphere, with cobalt nitrate, thiourea, and polyvinylpyrrolidone (PVP) as the cobalt, sulfur, and carbon sources, respectively.[68] At 900 °C, H_2S gas evolved from thiourea and reacted with the cobalt oxide intermediate to form Co_9S_8 nanoparticles, around which carbonized PVP formed an amorphous carbon layer (Figure 2a–c). Compared with bare $Co_{1-x}S$ powder, the Co_9S_8-carbon composite exhibited better cyclability and rate performance (Figure 2d, e). Choi and co-worker synthesized SnS-C composite microspheres by spray pyrolysis at different temperatures.[69] The SnS-C composite microspheres exhibited hierarchical structures regardless of the synthesis temperature (Figure 2f). Plate-like SnS was formed outside the carbon microspheres at the preparation temperature of 700 °C (Figure 2g, h), whereas cubic-like SnS formed at 900 °C as a result of Ostwald ripening (Figure 2i, j). Chen et al. synthesized mesoporous MoS_2/C microspheres by one-pot spray pyrolysis under an Ar atmosphere with thiourea as a sulfur source.[70] By the same principle, H_2S gas from thiourea reacted with MoO_4^{2-} to produce MoS_2 nanosheets, and the gas evolution during the process favored the formation of mesoporous MoS_2/C microspheres (Figure 3a–d). The same group also reported the synthesis of SnS nanoparticles embedded in carbon spheres (SnS/C) by using a similar method (Figure 3g–i).[71] In both cases, the carbon matrix minimized the restacking and aggregation of MoS_2 and SnS nanosheets/nanoparticles during cycling, which contributed to the stable cycling performance (Figure 3f, k) and rate (Figure 3e, j). Choi et al. proposed the direct synthesis of 3D MoS_2-graphene microspheres, which consisted of multiple nanospheres, by spray

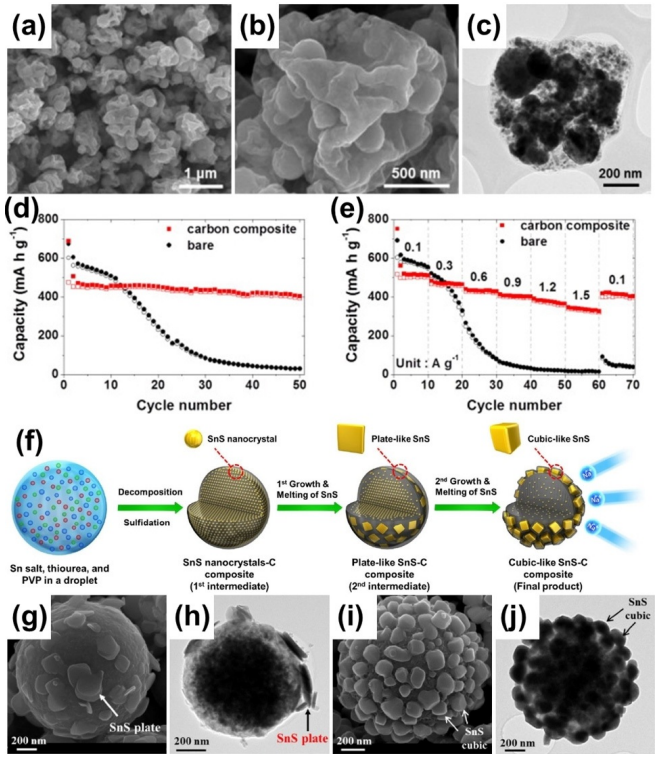

Figure 2. a, b) SEM and c) TEM images of the Co_9S_8-carbon composite synthesized by one-pot spray pyrolysis. d) Cycling performance at a current density of 0.5 A g^{-1} and e) rate performance of the Co_9S_8-carbon composite and bare $Co_{1-x}S$ powder. Reproduced with permission.[68] Copyright 2015, Elsevier. f) Schematic diagram of the formation of SnS-C composite microspheres by one-pot spray pyrolysis. g) SEM and h) TEM images of SnS-C composite microspheres prepared at 700 °C. i) SEM and j) TEM images of SnS-C composite microspheres prepared at 900 °C. Reproduced with permission.[69] Copyright 2015, Springer.

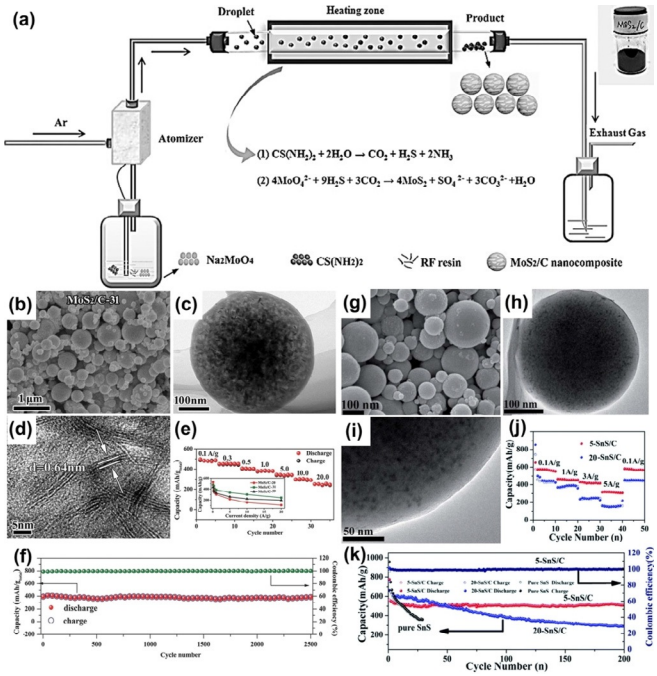

Figure 3. a) Schematic diagram of the preparation of mesoporous MoS_2/C microspheres and the corresponding b) SEM and c, d) TEM images, e) rate performance, and f) cycling performance at a current density of 1.0 A g^{-1}. Reproduced with permission.[70] Copyright 2015, Wiley-VCH. g) SEM and h, i) TEM images of SnS/C and the corresponding j) rate performance and k) cycling performance at a current density of 1.0 A g^{-1}. Reproduced with permission.[71] Copyright 2016, Royal Society of Chemistry.

pyrolysis (Figure 4a–d).[72] $(NH_4)_2MoS_4$ was used to obtain MoS_2 without dissolving an additional sulfur source in the spray solution. 3D graphene microspheres, which were incorporated with MoS_2 nanosheets, were obtained by using polystyrene nanobeads that could be completely decomposed under an inert atmosphere. The low stacking of MoS_2 layers lowered the barrier for Na^+ insertion and the empty spaces in graphene alleviated the volume expansion and provided fast electron-transfer pathways during cycling. As a result, 3D MoS_2-graphene composite microspheres could deliver a stable reversible capacity of 323 mA h g^{-1} during the 600th cycle at a current density of 1.5 A g^{-1} (Figure 4e, f). Kalluri et al. prepared MoS_2-graphene hierarchical microspheres by spray drying a colloidal solution that contained exfoliated MoS_2 nanosheets and graphene oxide (Figure 4g–j).[73] The miscibility and stability of the graphene oxide and MoS_2 nanosheets in aqueous solution played an important role in the formation of a sandwich-like structure. Such hierarchical microstructures could present excellent cycling stability, and showed 93% capacity retention after 500 cycles at a current density of 1 A g^{-1} (Figure 4k). The direct synthesis of metal sulfides by using one-pot spray pyrolysis is sometimes challenging owing to the short retention time of the particle in the furnace. Consequently, post-treatment sulfidation of the as-sprayed powder has been proposed as an efficient technique to synthesize a wide variety of metal sulfides with controllable compositions. Choi et al. synthesized WS_2-decorated 3D reduced graphene oxide microspheres (WS_2-3D RGO) by sulfidation of WO_3-3D RGO at 400 °C for 12 h in the presence of 10% H_2/Ar gas with thiourea as the sulfur source (Figure 5a).[74] WO_3 nanocrystals were converted into few-layer WS_2 nanosheets after the sulfidation process (Figure 5b–e). In addition, Lee et al. synthesized crumpled FeS-reduced graphene oxide (FeS-rGO) by sulfidation of Fe_3O_4-rGO at 250 °C (Figure 5f–k).[75] Both studies used rGO to restrict crystal growth and give structural stability, and exhibited stable electrochemical performance of the products (Table 1). Park et al. synthesized nickel sulfide hollow nanospheres/rGO composite powders by spray drying and subsequent post-treatments (Figure 6a).[76] The spray-dried Ni acetate/GO composite powder was reduced to Ni/rGO composite under an H_2/Ar atmosphere (Figure 6b, c), followed by sulfidation at 300 °C for 12 h. Interestingly, hollow nickel sulfide nanospheres were formed by the nanoscale Kirkendall effect during the sulfidation process; that is, the outward diffusion of Ni cations (with small radii) proceeded faster than the inward diffusion of S anions (with larger radii; Figure 6d, e). The structural stability of the hollow nickel sulfide nanospheres/rGO composites was demonstrated by superior long-term cycling and rate performance compared with dense nickel sulfide nanospheres/rGO composites, formed by direct sulfidation of Ni acetate/GO composite powder (Figure 6f, g).

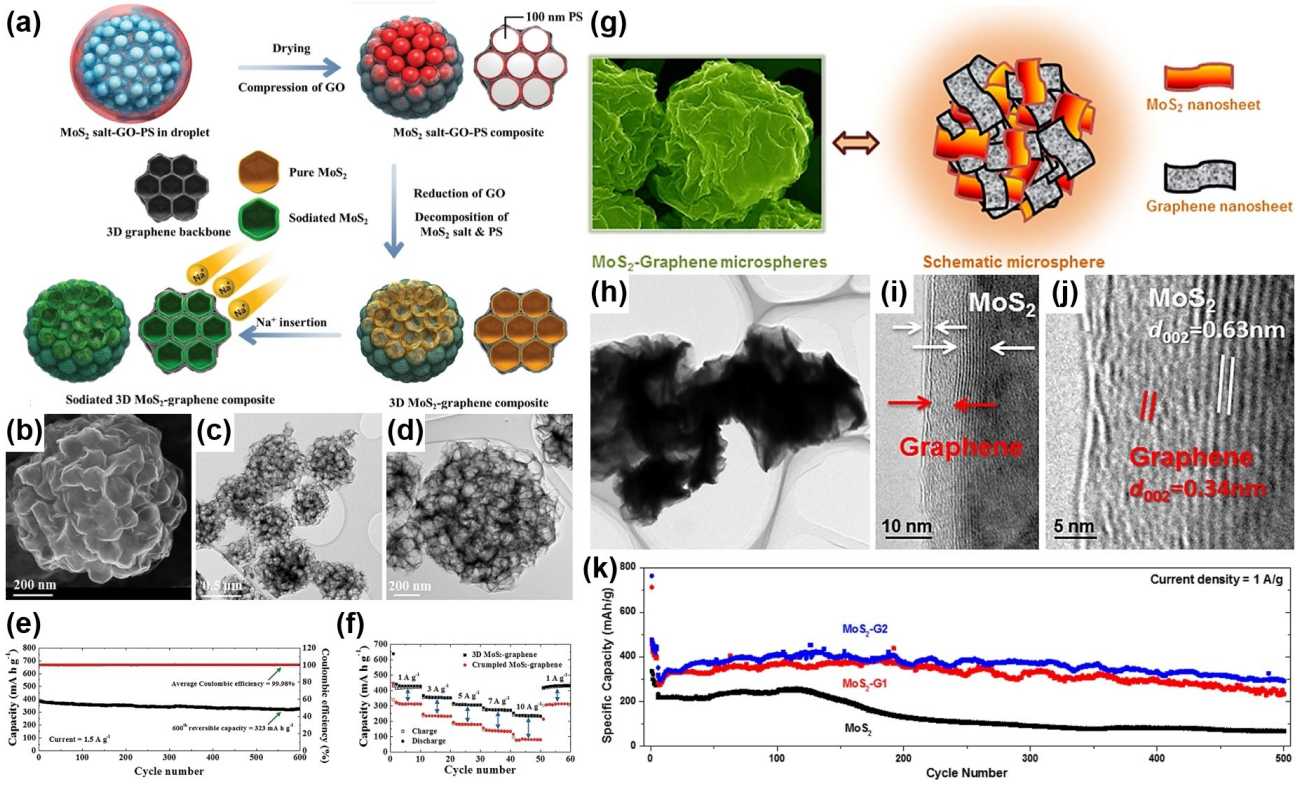

Figure 4. a) Schematic diagram of the formation of 3D MoS_2-graphene composite microspheres. b) SEM and c, d) TEM images of 3D MoS_2-graphene composite microspheres and the corresponding e) cycling performance and f) rate performance. Reproduced with permission.[72] Copyright 2015, Wiley-VCH. g) Schematic diagram of MoS_2-graphene hierarchical microspheres prepared by spray drying. h)–j) TEM images of MoS_2-graphene hierarchical microspheres and the corresponding k) cycling performance. Reproduced with permission.[73] Copyright 2015, Nature Publishing Group.

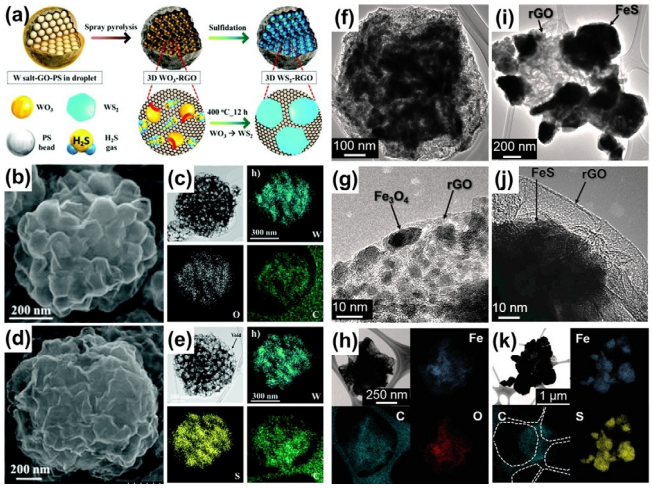

Figure 5. a) Schematic diagram for the formation of WS_2-3D RGO by spray pyrolysis and post-treatment. b) SEM and c) TEM and elemental mapping images of WO_3-3D RGO. d) SEM and e) TEM and elemental mapping images of WS_2-3D RGO after sulfidation at 400 °C. Reproduced with permission.[74] Copyright 2015, Royal Society of Chemistry. f, g) TEM and h) elemental mapping images of Fe_3O_4-rGO. i, j) TEM and k) elemental mapping images of FeS-rGO. Reproduced with permission.[75] Copyright 2016, Wiley-VCH.

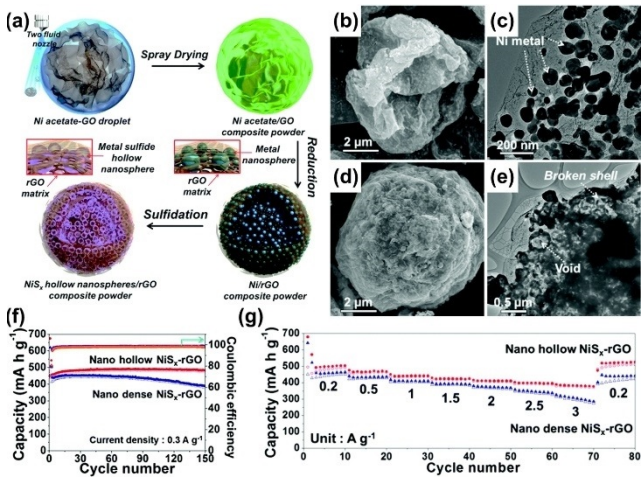

Figure 6. a) Schematic diagram of the formation of nickel sulfide hollow nanospheres/rGO composite powders by spray drying and post-treatments. b) SEM and c) TEM images of the Ni/rGO composite reduced from Ni acetate/GO composite powder prepared by spray drying. d) SEM and e) TEM images of nickel sulfide hollow nanospheres/rGO composite obtained after nanoscale Kirkendall diffusion. f) Cycling performance and g) rate performance of nickel sulfide hollow and dense nanospheres/rGO composite. Reproduced with permission.[76] Copyright 2015, Royal Society of Chemistry.

The same strategy has been applied to the synthesis of many other novel nanostructured metal sulfide/carbon composites. Kang and co-workers reported the synthesis of yolk–shell-structured $(Fe_{0.5}Ni_{0.5})_9S_8$ by sulfidation of oxide precursors.[77] Spray pyrolysis is a specialized method for the facile and rapid synthesis of yolk–shell-structured metal oxides

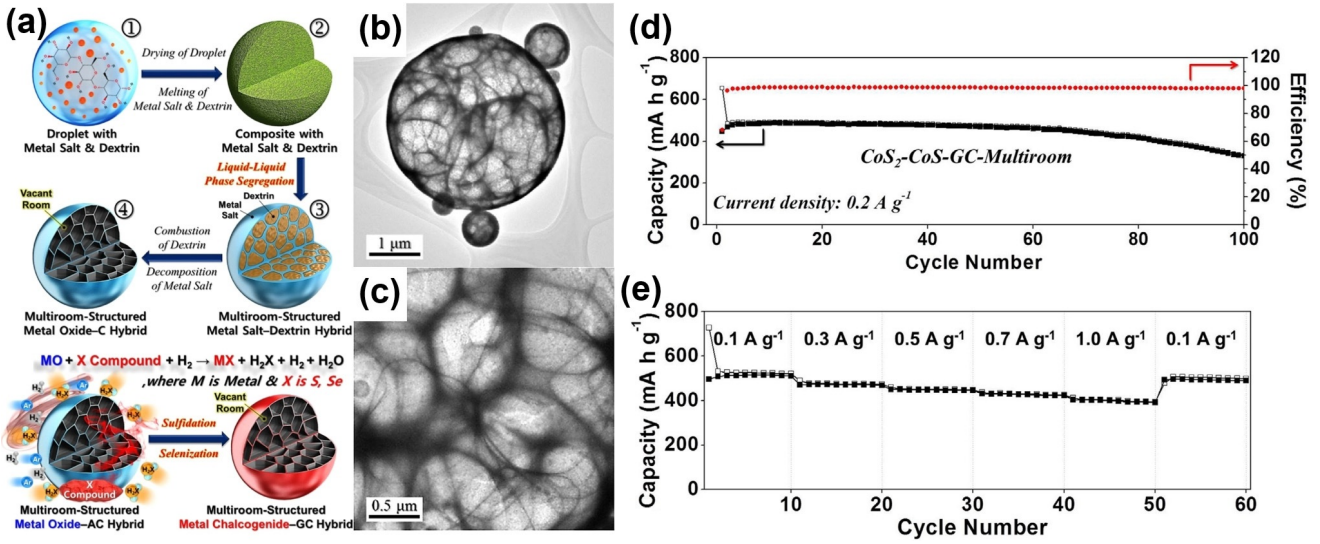

Figure 7. a) Schematic diagram for the formation of multiroom-structured metal compound-carbon hybrids. b,c) TEM images of multiroom-structured cobalt sulfide/carbon. d) Cycling performance at a current density of 0.2 A g^{-1} and e) rate performance of multiroom-structured cobalt sulfide/carbon. Reproduced with permission.[78] Copyright 2016, Elsevier.

through the repeated decomposition and contraction of metal oxide/carbon intermediates.[45] A yolk–shell structure, coupled with the uniform nanoscale mixing of two metal sulfides, buffered the instability of the electrode during cycling and delivered improved electrochemical performance. Cho et al. introduced the synthesis of multiroom-structured metal compound-carbon hybrids by spray pyrolysis for the first time (Figure 7).[78]

By controlling the amount of dextrin in the spray solution, multiroom-structured metal Co oxide-carbon could be produced (Figure 7a–c). However, the electrochemical performance of the multiroom-structured cobalt sulfide/carbon, one of the target materials chosen in this study, was not as satisfactory, probably because of the weak internal walls (Figure 7d,e). Park et al. reported similarly structured multicomponent MoS_2-Ni_9S_8-C microspheres obtained by spray drying and subsequent sulfidation.[79] Kim et al. used NaCl as a washable template to produce metal sulfide/carbon microspheres with cubic nanorooms (MeS_x/C-NR; Figure 8a).[80] The authors reported that this method can be generalized for the synthesis of any metal sulfide/carbon composites, such as MoS_2/C-NR, SnS/C-NR, and FeS_2/C-NR (Figure 8b–h). Notably, MoS_2/C-NR exhibited a stable reversible capacity of 385 mA h g^{-1} after 350 cycles at a current density of 0.5 A g^{-1}, and a high rate capability of 287 mA h g^{-1} at a current density of 7.0 A g^{-1} (Table 1). The excellent electrochemical performance was derived from the increased active surface area for electrochemical reaction by the introduction of numerous nanorooms without compromising the structural stability.

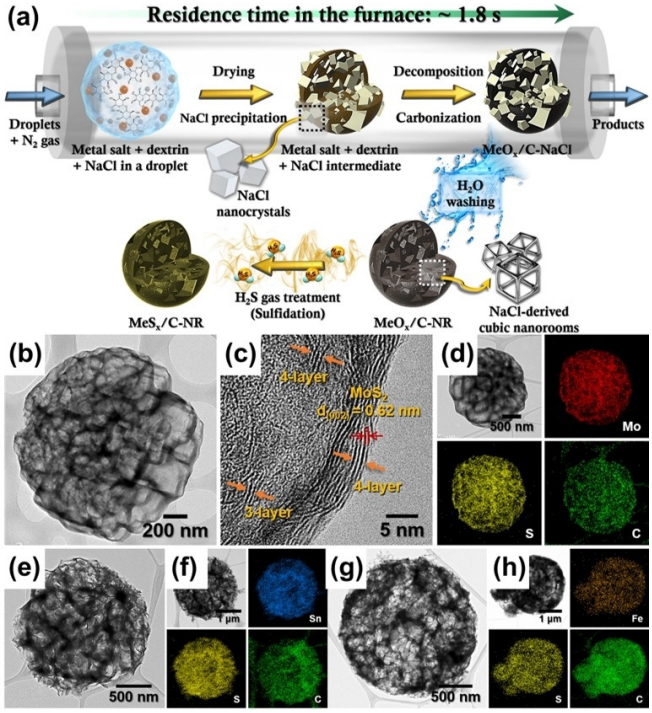

Figure 8. a) Schematic diagram of the synthesis of MeS_x/C-NR by spray pyrolysis and subsequent treatments. b,c) TEM and d) elemental mapping images of MoS_2/C-NR. e) TEM and f) elemental mapping images of SnS/C-NR. g) TEM and h) elemental mapping images of FeS_2/C-NR. Reproduced with permission.[80] Copyright 2019, Royal Society of Chemistry.

2.2. Metal selenides

Although metal selenides have lower theoretical capacities than their oxide counterparts because of the relatively heavier atomic mass of Se, they often exhibit higher capacities owing to reduced energy consumption during the conversion reaction. This is attributed to the lower formation enthalpy of Na_2Se (−342 kJ mol^{-1}) compared with that of Na_2O (−418 kJ mol^{-1}) and the weaker binding energy of the M–Se bond due to the decreased electronegativity of Se.[23,24] In addition, metal selenides exhibit less polarization than their oxide and sulfide counterparts;[21] thus, they are another class of

promising electrode materials for SIBs. Spray pyrolysis and spray drying have been used for the synthesis of nanostructured metal chalcogenide materials.

As discussed above, metal selenides can also be synthesized by using an aerosol-assisted process with a solution that contains a Se species. Selenium oxide, a water-soluble solute, has been used as a Se source. For example, Park et al. reported the synthesis of $CoSe_x$-rGO composite powder and SnSe nanoplates by using one-pot spray pyrolysis (Figure 9a–h).[81,82] To synthesize metal selenides with the desired morphologies, the authors attempted to optimize the process conditions by controlling the ratio of metal salts and SeO_2, the reactor temperature, and the retention time in the reactor. During the process, the salts decomposed and were reduced to metal and Se species. Then, the reduced metal and Se underwent an alloying process. Excess Se was converted to H_2Se and Se gases, which also reacted with the metal to form metal selenides. As a result, the synthesized samples under optimized conditions delivered enhanced electrochemical performance (Figure 9d, h). Furthermore, the authors also synthesized spherical $FeSe_2$-amorphous carbon composite powders by using spray drying and post-treatment (Figure 9i–k).[83] During post-treatment, H_2Se gas evolved from the precursor reacted with Fe to form $FeSe_2$, which occurred simultaneously with the carbonization of dextrin. The cycling performance was optimized by controlling the amount of dextrin in the precursor, and the product exhibited better stability than $FeSe_2$ without carbon (Figure 9l).

However, the one-pot synthesis of metal selenides requires an excess of SeO_2 and prolonged retention time in the reactor for the particles. This causes a deformation of the powder morphology owing to a tremendous amount of gas evolution and significant crystal growth of metal selenide nanoparticles. Therefore, post-treatment with Se powder could be a versatile synthesis route for nanostructured metal selenides. Ko et al. introduced the synthesis of yolk–shell molybdenum selenide and hollow cobalt selenide microspheres by a simple selenization of their oxide precursors at 300 °C.[84,85] The synthesized powders maintained their original morphology without significant sintering, which demonstrated the effectiveness of selenization by post-treatment. However, the cycling stability and rate performance were not satisfactory, mainly owing to the absence of a carbon matrix. Therefore, metal selenides incorporated with carbonaceous materials have been widely studied. Choi et al. synthesized fullerene-like $MoSe_2$ nanoparticle-embedded carbon nanotube (CNT) balls (Figure 10a–d).[86] The 3D porous CNT network prevented the aggregation of $MoSe_2$ nanoparticles and improved the electrical conductivity of the material, which resulted in good cycling stability over 250 cycles and a high discharge capacity of 255 mA h g^{-1} at a current density of 5.0 A g^{-1} (Figure 10e, f). Cho et al. used graphene to incorpo-

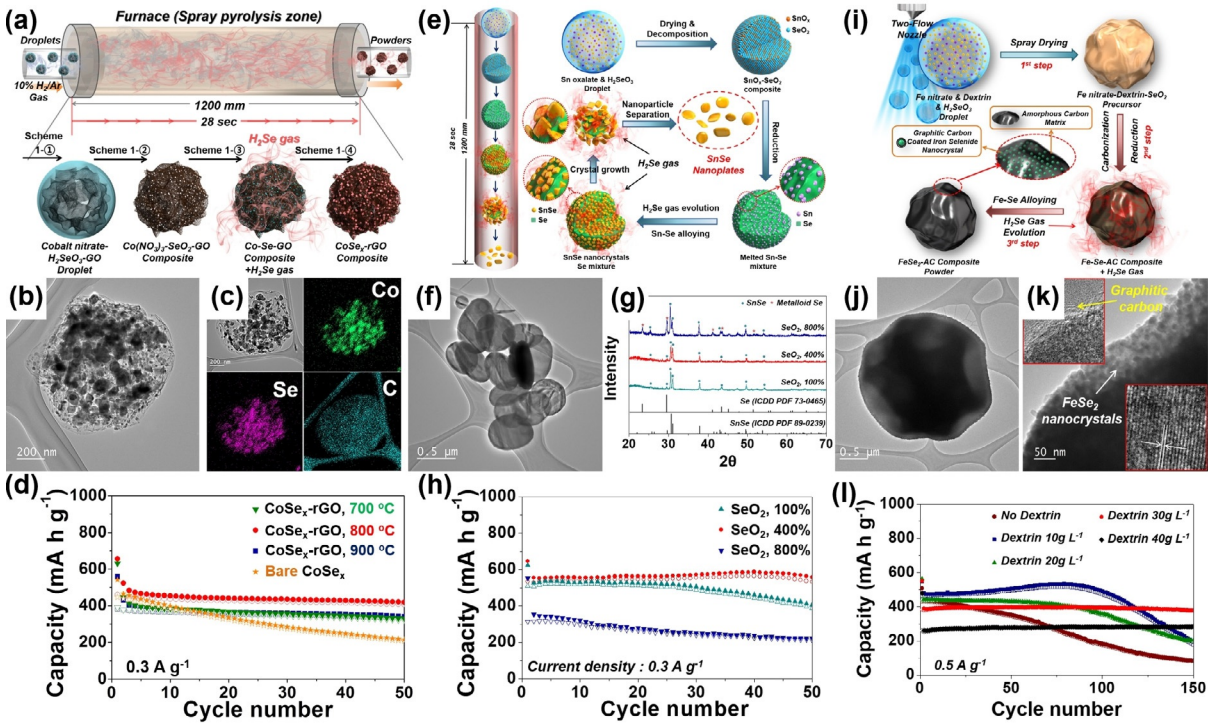

Figure 9. a) Schematic diagram of the formation of $CoSe_x$-rGO composite powder by one-pot spray pyrolysis. b) TEM and c) elemental mapping images of $CoSe_x$-rGO composite powder prepared at 800 °C. d) Cycling performance of $CoSe_x$-rGO composite powders prepared at various temperatures. Reproduced with permission.[81] Copyright 2016, Wiley-VCH. e) Schematic diagram of the formation of SnSe nanoplates by one-pot spray pyrolysis. f) TEM image of SnSe nanoplates prepared from a spray solution with 400% stoichiometric SeO_2. g) XRD patterns and h) cycling performance at a current density of 0.3 A g^{-1} of powders prepared by spray pyrolysis from spray solutions with various excesses of SeO_2. Reproduced with permission.[82] Copyright 2016, Royal Society of Chemistry. i) Schematic diagram of the formation of $FeSe_2$-amorphous carbon composite powders by spray drying and post-treatment. j, k) TEM images of $FeSe_2$-amorphous carbon composite powder. l) Cycling performance of $FeSe_2$-amorphous carbon composite and bare $FeSe_2$ powder prepared from spray solutions that contained various amounts of dextrin. Reproduced with permission.[83] Copyright 2016, Elsevier.

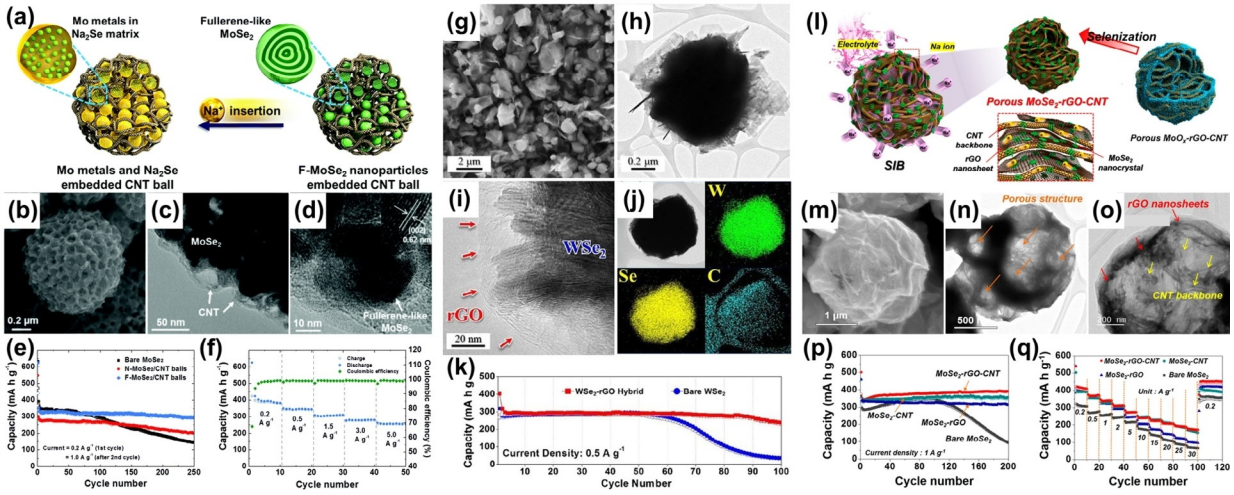

Figure 10. a) Schematic diagram of the synthesis of fullerene-like $MoSe_2$ nanoparticles-embedded CNT balls. b) SEM and c, d) TEM images of fullerene-like $MoSe_2$ nanoparticles-embedded CNT balls. e) Cycling performance at a current density of 1.0 A g^{-1} after the 2nd cycle and f) rate performance of fullerene-like $MoSe_2$ nanoparticles-embedded CNT balls. Reproduced with permission.[86] Copyright 2016, Royal Society of Chemistry. g) SEM, h, i) TEM, and j) elemental mapping images of the mesoporous WSe_2-rGO hybrid. k) Cycling performance of WSe_2-rGO hybrid and bare WSe_2 at a current density of 0.5 A g^{-1}. Reproduced with permission.[87] Copyright 2018, Elsevier. l) Schematic diagram of the formation of $MoSe_2$-rGO-CNT microspheres. m) SEM and n, o) TEM images of $MoSe_2$-rGO-CNT microspheres. p) Cycling performance at a current density of 1 A g^{-1} and q) rate performance of bare $MoSe_2$ and $MoSe_2$-carbon composites. Reproduced with permission.[88] Copyright 2017, American Chemical Society.

rate WSe_2 (Figure 10g–j).[87] The mesoporous WSe_2-rGO hybrid showed improved cycling stability compared with bare WSe_2 (Figure 10k). Park et al. synthesized $MoSe_2$-embedded CNT-rGO ($MoSe_2$-rGO-CNT) microspheres by using spray pyrolysis (Figure 10l–o).[88] The synergistic effect of CNT and rGO minimized the crystal growth of $MoSe_2$ during the selenization and restacking of $MoSe_2$ nanocrystals and graphene nanosheets. As a result, $MoSe_2$-rGO-CNT exhibited improved electrochemical performance compared with $MoSe_2$-rGO and $MoSe_2$-CNT microspheres (Figure 10p, q). Furthermore, Park et al. incorporated a metal–organic framework (MOF) with CNT microspheres synthesized by spray pyrolysis.[89] After depositing a Co-based MOF (ZIF-67) on the CNT microspheres, the authors selenized the composite powder to produce N-doped carbon-coated $CoSe_2$ nanorods supported on porous CNT ($CoSe_2$@NC-NR/CNT) microspheres. Coupled with the porous CNT network, which greatly improved the electrical conductivity and structural robustness of the material, $CoSe_2$@NC-NR/CNT showed better cycling stability and rate performance than $CoSe_2$@NC produced by the selenization of ZIF-67 alone. Multiroom-structured metal selenide/carbon composites were also introduced. Kim et al. reported $CoSe_2$-$MoSe_2$-C microspheres that contained tens of vacant nanorooms, formed by selenization of $CoMoO_4$/C microspheres (Figure 11a–d).[90] The decomposition of dextrin "islands" embedded in molten metal salts was the key to nanoroom construction. The microspheres exhibited long-term cycling stability and high rate performance when compared with the dense-structured microspheres owing to the synergistic effects between the metal selenides and the conductive carbon matrix with internal nanorooms (Figure 11e, f). Choi et al. introduced a salt-templated approach to form interconnected multicavities within hollow iron selenide/graphitic carbon microspheres (H-$FeSe_2$/GC).[91] Numerous cavities were formed by the removal of NaCl nanocrystals, and hollow $FeSe_2$ nanospheres were formed by the Kirkendall effect during post-treatment (Figure 11g–j). These characteristic features contributed to enhanced electrochemical performance, with stable cycling performance over 200 cycles and a reversible capacity retention of 88% (Figure 11k).

2.3. Metal tellurides

Tellurium (Te) is a chalcogen that exhibits electrical conductivity (200 S m^{-1}) several orders of magnitude higher than Se (10^{-4} S m^{-1}) and high volumetric capacity on account of its high density.[92–94] Similar to sulfides and selenides, tellurides react with Na to produce a Na_2Te matrix as a discharge product.[95] Therefore, metal tellurides could be another promising anode material for SIBs, but to date they have not been as widely investigated as sulfides and selenides. Similar to the early stages of research into metal tellurides as anode material for LIBs,[92,93] metal telluride anodes for SIBs have been prepared by using the high-energy ball-milling process, which is a simple method to produce nanopowders with targeted stoichiometric compositions in a solid-state reaction. For example, cubic-crystal-structured SnTe/C was synthesized by a two-step ball-milling process under an Ar atmosphere.[96] The synthesized SnTe/C exhibited a high tap density of 2.02 g cm^{-3} and enhanced gravimetric/volumetric capacities of 316 mA h g^{-1} and 639 mA h cm^{-3}, respectively, after 100 cycles. An Sb_2Te_3-C composite was also synthesized by a two-step ball-milling process, and exhibited a high tap density of 2.05 g cm^{-3} and a reversible capacity of 373 mA h g^{-1} after 50 cycles at a current density of 50 mA g^{-1}.[97] The liquid-phase synthesis of other metal telluride/carbon materials, such as $CoTe_2$/graphene, $Cu_{1.75}Te$/C, and SnTe-rGO, has also been introduced.[94,98,99] However, the ball-milling process is not applicable to the synthesis of nanostructured metal telluride materials. Thus, spray

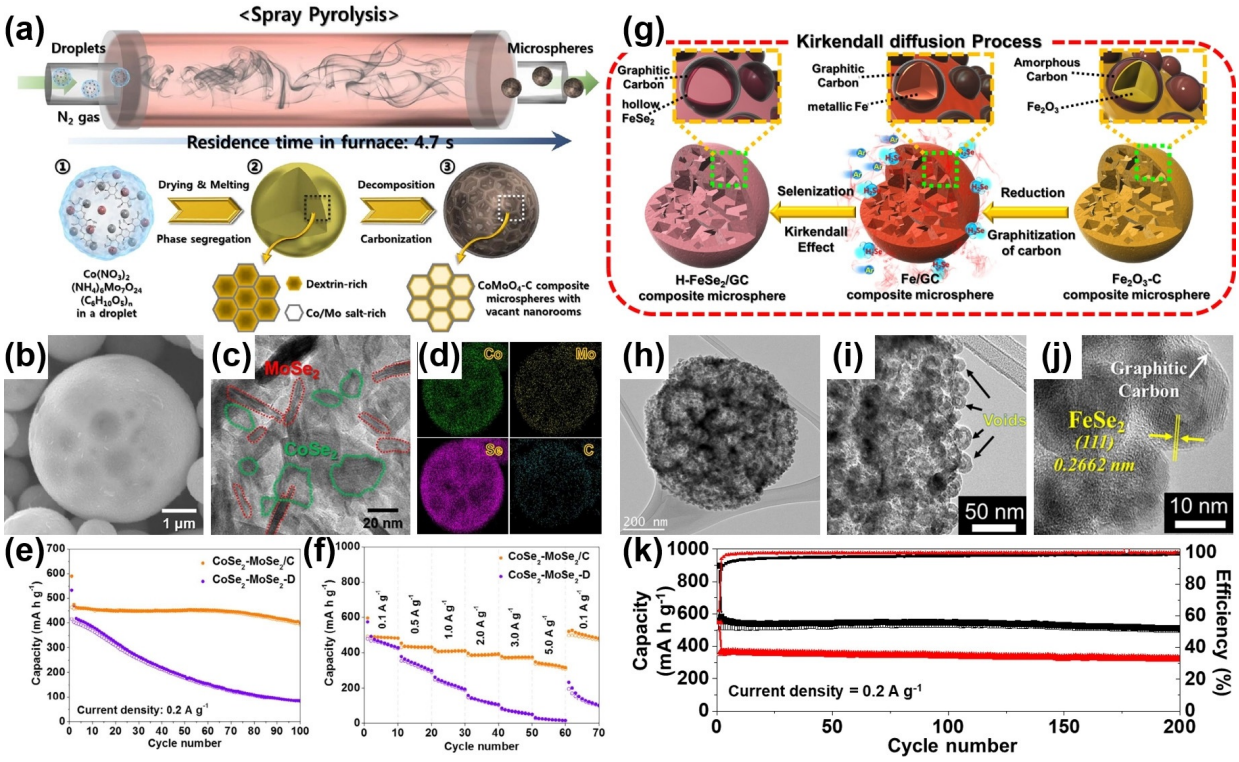

Figure 11. a) Schematic diagram of the formation of $CoMoO_4$/C microspheres with tens of vacant nanorooms by spray pyrolysis. b) SEM, c) TEM, and d) elemental mapping images of $CoSe_2$-$MoSe_2$-C microspheres with tens of vacant nanorooms obtained by the selenization of $CoMoO_4$/C microspheres, and the corresponding e) cycling performance and f) rate performance. Reproduced with permission.[90] Copyright 2017, Elsevier. g) The formation of H-$FeSe_2$/GC, and the corresponding h)–j) TEM images and k) cycling performance. Reproduced with permission.[91] Copyright 2018, Wiley-VCH.

pyrolysis has also been effectively employed in the synthesis of metal telluride/carbon composites with controlled morphology. The tellurization process was successfully conducted by generating H_2Te gas from Te metal powder. Unlike other methods, the composite maintained spherical morphology and metal telluride nanocrystals were homogeneously dispersed along the carbon support. $FeTe_2$-rGO hybrid microspheres were prepared by spray pyrolysis and subsequent tellurization (Figure 12a).[95]

Treatment with H_2Te gas transformed the as-sprayed Fe_3O_4-rGO microspheres into $FeTe_2$-rGO microspheres, in which $FeTe_2$ nanocrystals are embedded within the rGO sheets (Figure 12b,c). The authors confirmed the formation of Fe nanocrystals and Na_2Te as a result of a conversion reaction with Na by using ex situ XRD and TEM analyses (Figure 12f,g). The discharge capacity of the $FeTe_2$-rGO hybrid powders after 80 cycles was 293 mA h g^{-1} at a current density of 0.2 A g^{-1}, and the corresponding volumetric capacity was 2362 mA h cm^{-3}. $FeTe_2$-rGO hybrid powders had superior Na-ion storage properties compared with bare $FeTe_2$ powders, owing to their high structural stability and electrical conductivity (Figure 12d,e). Carbon@$MoTe_2$ core–shell microspheres were prepared by a tellurization process of C-MoO_x composite microspheres obtained by spray pyrolysis (Figure 13a).[100] At a higher tellurization temperature of 600 °C, all the $MoTe_2$ nanocrystals migrated outward to the surface of the microsphere by Ostwald ripening (Figure 13b,c). The discharge capacity of C@$MoTe_2$ powders after 200 cycles was 286 mA h g^{-1}. The high structural stability and well-developed 2D layer of $MoTe_2$ in the C@$MoTe_2$ microspheres provided superior Na-ion storage properties compared with C/$MoTe_2$ composite microspheres or bare $MoTe_2$ powder (Figure 13d,e). Unlike sulfides or selenides, tellurides are formed at a relatively higher temperature because the higher melting point of Te forces the generation of H_2Te gas above 450 °C,[95,100] which is not favorable for restricting crystal growth. However, the synthesis of metal tellurides by aerosol-assisted processes is still promising due to simplicity of morphology control and carbon hybridization. Therefore, further studies should be carried out towards the synthesis of advanced metal telluride materials.

3. Conclusion

Herein, we have summarized recent progress in the syntheses of nanostructured metal chalcogenide materials as anodes for SIBs by spray pyrolysis and spray drying. SIBs have recently been spotlighted as a viable alternative to LIBs. However, the development of anode materials for SIBs is challenging and far from satisfactory, mainly because of the larger ionic radius and slower diffusion kinetics of Na^+. Thus, it is important to develop appropriate anode materials for SIBs by numerous processes and strategies. Metal chalcogenides are considered to be promising anode materials for SIBs because they possess increased bond lengths and correspondingly weak binding energy, which reduces the energy consumption of the sodia-

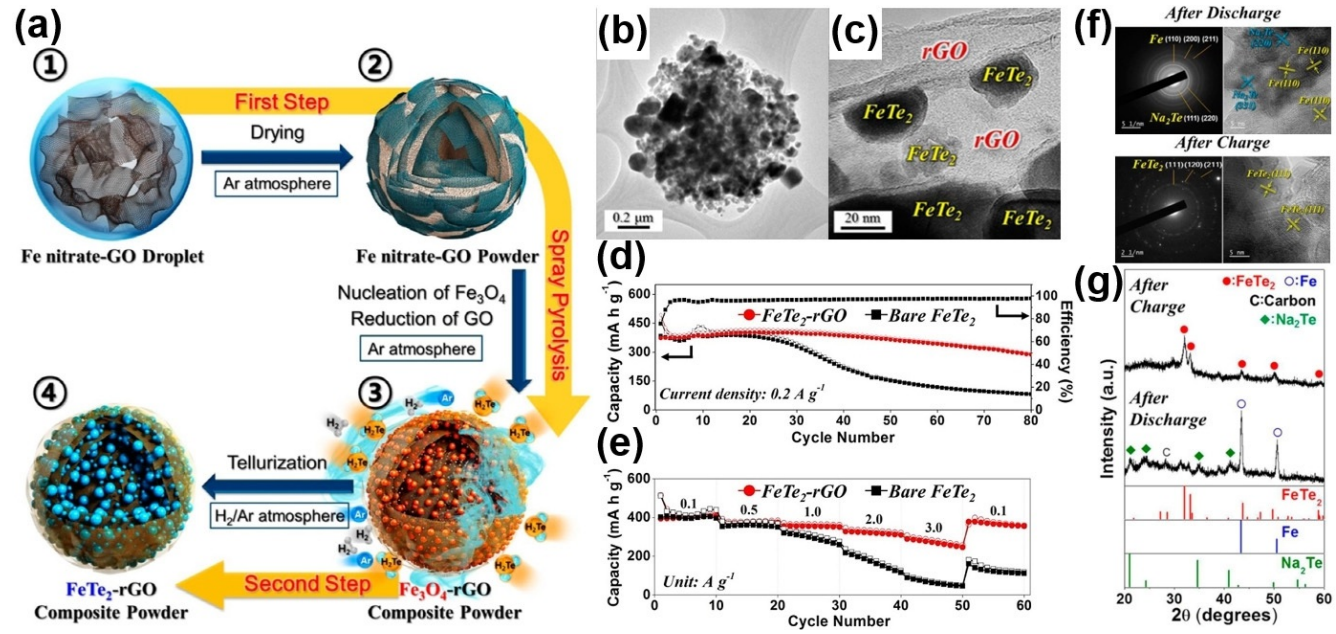

Figure 12. a) Formation of $FeTe_2$-rGO powder, and the corresponding b,c) TEM images, d) cycling performance, and e) rate performance. f) ex situ SAED patterns and TEM images and the corresponding g) XRD patterns of the reaction products after the first full discharge and charge processes. Reproduced with permission.[95] Copyright 2016, American Chemical Society.

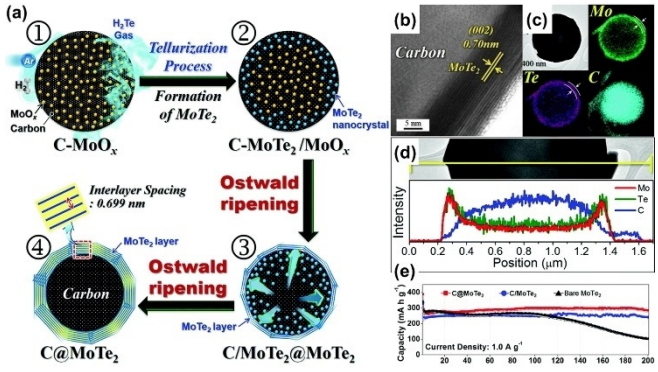

Figure 13. a) Formation of C@$MoTe_2$ composite microspheres, and the corresponding b) TEM and c) elemental mapping images, d) line profiles, and e) cycling performance. Reproduced with permission.[100] Copyright 2017, Royal Society of Chemistry.

tion/desodiation reaction. Furthermore, the discharge products (Na_2S and Na_2Se for sulfides and selenides, respectively) afford better electrical conductivity and lower formation enthalpies than Na_2O. However, several challenges, such as low reversible capacity, cycling, and rate performance, need to be overcome for the practical applications of metal chalcogenide material anodes in SIBs. For this reason, spray processes, such as spray pyrolysis and spray drying, combined with diverse mechanisms, have been applied to synthesize metal chalcogenide materials with ideal compositions, crystallite sizes, and desired nanostructures by simply adding additives to the spray solution, controlling the parameters during the spray process, and/or applying additional post-treatments. The synthesis of metal chalcogenide materials by spray processes has reportedly been achieved by reactions between the host metal/metal oxide and gaseous compounds that contain chalcogen anions at a certain temperature. As a result, diverse nanostructures with various structures and compositions, such as hollow, porous, yolk–shell, hierarchical, and multiroom, with carbon hybridization, such as amorphous carbon, graphitic carbon, N-doped carbon, mesoporous rGO, and CNTs, have been proposed for SIB anodes obtained through spray processes. Therefore, the resulting nanostructures exhibited increased active surface area, electrical conductivity, and mechanical stability, and shortened Na^+ diffusion length and electron transport pathways during the sodiation/desodiation reaction, which greatly improved the sodium-ion storage properties of the anodes.

This review suggests that spray processes have found many applications in the preparation of metal chalcogenide anode materials for SIBs, which require sophisticated nanostructures or multicomposite materials, mainly owing to their ability to form rational nanostructures. However, there are still some challenges remaining for further improvements in the preparation of metal chalcogenide anode materials by using spray processes. During the processes, particularly spray pyrolysis, a series of complicated physical and chemical reactions occur sequentially or simultaneously, which makes detailed architecture formation mechanisms difficult to understand. Thus, future efforts should concentrate on experimental and theoretical investigations into powder formation mechanisms during pyrolysis. Additionally, from an industrial/commercial point of view, the effects of operating parameters to scale up the synthesis process of metal chalcogenide materials should be taken into account. The main factors for synthesis include the starting materials, solvent, droplet generator, reactor, carrier gas, and heat source. Finally, it is necessary to explore newly designed metal chalcogenide anode materials optimized for high-per-

formance SIBs, which would make the spray process more attractive as a tool for the synthesis of electrode materials for the next generation of SIBs.

Acknowledgements

This work was supported by a National Research Foundation of Korea (NRF) grant funded by the Korea government (MSIP; no. 2017R1A2B2008592 2, 2018R1A4A1024691, and 2017R1D1A1B03034473).

Conflict of interest

Please check! - The authors declare no conflict of interest.

Keywords: anode materials · metal chalcogenides · nanostructures · sodium ion batteries · spray processes

[1] N. S. Choi, Z. Chen, S. A. Freunberger, X. Ji, Y. K. Sun, K. Amine, G. Yushin, L. F. Nazar, J. Cho, P. G. Bruce, *Angew. Chem. Int. Ed.* **2012**, *51*, 9994 – 10024; *Angew. Chem.* **2012**, *124*, 10134 – 10166.
[2] D. Larcher, J.-M. Tarascon, *Nat. Chem.* **2015**, *7*, 19 – 29.
[3] M. Li, J. Lu, Z. Chen, K. Amine, *Adv. Mater.* **2018**, *30*, 1800561.
[4] Y. Wang, B. Liu, Q. Li, S. Cartmell, S. Ferrara, Z. D. Deng, J. Xiao, *J. Power Sources* **2015**, *286*, 330 – 345.
[5] M. Winter, B. Barnett, K. Xu, *Chem. Rev.* **2018**, *118*, 11433 – 11456.
[6] G. Zubi, R. Dufo-López, M. Carvalho, G. Pasaoglu, *Renewable Sustainable Energy Rev.* **2018**, *89*, 292 – 308.
[7] M. D. Slater, D. Kim, E. Lee, C. S. Johnson, *Adv. Funct. Mater.* **2013**, *23*, 947 – 958.
[8] N. Yabuuchi, K. Kubota, M. Dahbi, S. Komaba, *Chem. Rev.* **2014**, *114*, 11636 – 11682.
[9] H. Pan, Y.-S. Hu, L. Chen, *Energy Environ. Sci.* **2013**, *6*, 2338 – 2360.
[10] D. Kundu, E. Talaie, V. Duffort, L. F. Nazar, *Angew. Chem. Int. Ed.* **2015**, *54*, 3431 – 3448; *Angew. Chem.* **2015**, *127*, 3495 – 3513.
[11] Y. Fang, X. Y. Yu, X. W. Lou, *Angew. Chem. Int. Ed.* **2017**, *56*, 5801 – 5805; *Angew. Chem.* **2017**, *129*, 5895 – 5899.
[12] X. Xiong, W. Luo, X. Hu, C. Chen, L. Qie, D. Hou, Y. Huang, *Sci. Rep.* **2015**, *5*, 9254.
[13] J. Kim, H. Kim, K. Kang, *Adv. Energy Mater.* **2018**, *8*, 1702646.
[14] P. G. Bruce, B. Scrosati, J. M. Tarascon, *Angew. Chem. Int. Ed.* **2008**, *47*, 2930 – 2946; *Angew. Chem.* **2008**, *120*, 2972 – 2989.
[15] H. Kang, Y. Liu, K. Cao, Y. Zhao, L. Jiao, Y. Wang, H. Yuan, *J. Mater. Chem. A* **2015**, *3*, 17899 – 17913.
[16] W. Luo, F. Shen, C. Bommier, H. Zhu, X. Ji, L. Hu, *Acc. Chem. Res.* **2016**, *49*, 231 – 240.
[17] Y. Kim, K. H. Ha, S. M. Oh, K. T. Lee, *Chem. Eur. J.* **2014**, *20*, 11980 – 11992.
[18] A. Rudola, K. Saravanan, C. W. Mason, P. Balaya, *J. Mater. Chem. A* **2013**, *1*, 2653 – 2662.
[19] Y. Wen, K. He, Y. Zhu, F. Han, Y. Xu, I. Matsuda, Y. Ishii, J. Cumings, C. Wang, *Nat. Commun.* **2014**, *5*, 4033.
[20] B. Xiao, T. Rojo, X. Li, *ChemSusChem* **2019**, *12*, 133 – 144.
[21] B. Farbod, K. Cui, W. P. Kalisvaart, M. Kupsta, B. Zahiri, A. Kohandehghan, E. M. Lotfabad, Z. Li, E. J. Luber, D. Mitlin, *ACS Nano* **2014**, *8*, 4415 – 4429.
[22] Y. Kim, Y. Park, A. Choi, N. S. Choi, J. Kim, J. Lee, J. H. Ryu, S. M. Oh, K. T. Lee, *Adv. Mater.* **2013**, *25*, 3045 – 3049.
[23] F. Klein, B. Jache, A. Bhide, P. Adelhelm, *Phys. Chem. Chem. Phys.* **2013**, *15*, 15876 – 15887.
[24] P. Ge, C. Zhang, H. Hou, B. Wu, L. Zhou, S. Li, T. Wu, J. Hu, L. Mai, X. Ji, *Nano Energy* **2018**, *48*, 617 – 629.
[25] Q. Zhou, L. Liu, Z. Huang, L. Yi, X. Wang, G. Cao, *J. Mater. Chem. A* **2016**, *4*, 5505 – 5516.
[26] Y. Xiao, S. H. Lee, Y. K. Sun, *Adv. Energy Mater.* **2017**, *7*, 1601329.
[27] Y. Zhang, Q. Zhou, J. Zhu, Q. Yan, S. X. Dou, W. Sun, *Adv. Funct. Mater.* **2017**, *27*, 1702317.
[28] Z. Hu, Q. Liu, S. L. Chou, S. X. Dou, *Adv. Mater.* **2017**, *29*, 1700606.
[29] K. Zhang, M. Park, L. Zhou, G. H. Lee, W. Li, Y. M. Kang, J. Chen, *Adv. Funct. Mater.* **2016**, *26*, 6728 – 6735.
[30] C. Tang, X. Wei, X. Cai, Q. An, P. Hu, J. Sheng, J. Zhu, S. Chou, L. Wu, L. Mai, *ACS Appl. Mater. Interfaces* **2018**, *10*, 19626 – 19632.
[31] Y. Pan, X. Cheng, L. Gong, L. Shi, Y. Deng, H. Zhang, *J. Mater. Chem. A* **2018**, *6*, 18967 – 18978.
[32] Z. Deng, H. Jiang, C. Li, *Small* **2018**, *14*, 1800148.
[33] H. Zhang, I. Hasa, S. Passerini, *Adv. Energy Mater.* **2018**, *8*, 1702582.
[34] Y. Liang, W. H. Lai, Z. Miao, S. L. Chou, *Small* **2018**, *14*, 1702514.
[35] Y. Lu, Y. Lu, Z. Niu, J. Chen, *Adv. Energy Mater.* **2018**, *8*, 1702469.
[36] M.-S. Balogun, Y. Luo, W. Qiu, P. Liu, Y. Tong, *Carbon* **2016**, *98*, 162 – 178.
[37] Q. Wang, C. Zhao, Y. Lu, Y. Li, Y. Zheng, Y. Qi, X. Rong, L. Jiang, X. Qi, Y. Shao, D. Pan, B. Li, Y.-S. Hu, L. Chen, *Small* **2017**, *13*, 1701835.
[38] H. Fan, H. Yu, Y. Zhang, J. Guo, Z. Wang, H. Wang, N. Zhao, Y. Zheng, C. Du, Z. Dai, Q. Yan, J. Xu, *Energy Storage Mater.* **2018**, *10*, 48 – 55.
[39] W. Li, S. Hu, X. Luo, Z. Li, X. Sun, M. Li, F. Liu, Y. Yu, *Adv. Mater.* **2017**, *29*, 1605820.
[40] Y. Fang, X. Y. Yu, X. W. Lou, *Adv. Mater.* **2018**, *30*, 1706668.
[41] Y. Liu, X.-Y. Yu, Y. Fang, X. Zhu, J. Bao, X. Zhou, X. W. D. Lou, *Joule* **2018**, *2*, 725 – 735.
[42] J. Liu, P. Kopold, C. Wu, P. A. van Aken, J. Maier, Y. Yu, *Energy Environ. Sci.* **2015**, *8*, 3531 – 3538.
[43] J. H. Bang, K. S. Suslick, *Adv. Mater.* **2010**, *22*, 1039 – 1059.
[44] C. Boissiere, D. Grosso, A. Chaumonnot, L. Nicole, C. Sanchez, *Adv. Mater.* **2011**, *23*, 599 – 623.
[45] Y. J. Hong, M. Y. Son, Y. C. Kang, *Adv. Mater.* **2013**, *25*, 2279 – 2283.
[46] D. S. Jung, Y. N. Ko, Y. C. Kang, S. B. Park, *Adv. Powder Technol.* **2014**, *25*, 18 – 31.
[47] Y. Lu, N. Zhang, Q. Zhao, J. Liang, J. Chen, *Nanoscale* **2015**, *7*, 2770 – 2776.
[48] Y. Zhu, S. H. Choi, X. Fan, J. Shin, Z. Ma, M. R. Zachariah, J. W. Choi, C. Wang, *Adv. Energy Mater.* **2017**, *7*, 1601578.
[49] P. Nie, G. Xu, J. Jiang, H. Dou, Y. Wu, Y. Zhang, J. Wang, M. Shi, R. Fu, X. Zhang, *Small Methods* **2018**, *2*, 1700272.
[50] B. Vertruyen, N. Eshraghi, C. Piffet, J. Bodart, A. Mahmoud, F. Boschini, *Materials* **2018**, *11*, 1076.
[51] Y. Liang, H. Tian, J. Repac, S.-C. Liou, J. Chen, W. Han, C. Wang, S. Ehrman, *Energy Storage Mater.* **2018**, *13*, 8 – 18.
[52] A. B. D. Nandiyanto, K. Okuyama, *Adv. Powder Technol.* **2011**, *22*, 1 – 19.
[53] W. Y. Teoh, R. Amal, L. Mädler, *Nanoscale* **2010**, *2*, 1324 – 1347.
[54] R. Strobel, S. E. Pratsinis, *J. Mater. Chem.* **2007**, *17*, 4743 – 4756.
[55] Y. Wang, Y. Wu, A. Shirazi-Amin, P. Kerns, J. Fee, J. He, L. Jin, R. Maric, S. L. Suib, *ACS Appl. Energy Mater.* **2019**, *2*, 2370 – 2374.
[56] J. Leng, Z. Wang, J. Wang, H.-H. Wu, G. Yan, X. Li, H. Guo, Y. Liu, Q. Zhang, Z. Guo, *Chem. Soc. Rev.* **2019**, *48*, 3015 – 3072.
[57] P. Nie, Z. Le, G. Chen, D. Liu, X. Liu, H. B. Wu, P. Xu, X. Li, F. Liu, L. Chang, X. Zhang, Y. Lu, *Small* **2018**, *14*, 1800635.
[58] W. Qin, T. Chen, L. Pan, L. Niu, B. Hu, D. Li, J. Li, Z. Sun, *Electrochim. Acta* **2015**, *153*, 55 – 61.
[59] W. Qin, T. Chen, T. Lu, D. H. C. Chua, L. Pan, *J. Power Sources* **2016**, *302*, 202 – 209.
[60] W. Qin, D. Li, X. Zhang, D. Yan, B. Hu, L. Pan, *Electrochim. Acta* **2016**, *191*, 435 – 443.
[61] J. S. Cho, J.-S. Park, Y. C. Kang, *Nano Res.* **2017**, *10*, 897 – 907.
[62] W.-H. Ryu, J.-W. Jung, K. Park, S.-J. Kim, I.-D. Kim, *Nanoscale* **2014**, *6*, 10975 – 10981.
[63] Y. Wang, Y. Zhang, J. Shi, X. Kong, X. Cao, S. Liang, G. Cao, A. Pan, *Energy Storage Mater.* **2019**, *18*, 366 – 374.
[64] C. Wu, Y. Jiang, P. Kopold, P. A. van Aken, J. Maier, Y. Yu, *Adv. Mater.* **2016**, *28*, 7276 – 7283.
[65] L. Shen, Y. Wang, F. Wu, I. Moudrakovski, P. A. van Aken, J. Maier, Y. Yu, *Angew. Chem. Int. Ed.* **2019**, *58*, 7238 – 7243; *Angew. Chem.* **2019**, *131*, 7316 – 7321.
[66] X. Wang, Y. Chen, Y. Fang, J. Zhang, S. Gao, X. W. Lou, *Angew. Chem.* **2019**, *131*, 2701 – 2705.
[67] S. Wang, Y. Fang, X. Wang, X. W. Lou, *Angew. Chem.* **2019**, *131*, 770 – 773.

[68] Y. N. Ko, Y. C. Kang, *Carbon* **2015**, *94*, 85 – 90.
[69] S. H. Choi, Y. C. Kang, *Nano Res.* **2015**, *8*, 1595 – 1603.
[70] Y. Lu, Q. Zhao, N. Zhang, K. Lei, F. Li, J. Chen, *Adv. Funct. Mater.* **2016**, *26*, 911 – 918.
[71] J. Wang, Y. Lu, N. Zhang, X. Xiang, J. Liang, J. Chen, *RSC Adv.* **2016**, *6*, 95805 – 95811.
[72] S. H. Choi, Y. N. Ko, J. K. Lee, Y. C. Kang, *Adv. Funct. Mater.* **2015**, *25*, 1780 – 1788.
[73] S. Kalluri, K. H. Seng, Z. Guo, A. Du, K. Konstantinov, H. K. Liu, S. X. Dou, *Sci. Rep.* **2015**, *5*, 11989.
[74] S. H. Choi, Y. C. Kang, *Nanoscale* **2015**, *7*, 3965 – 3970.
[75] S. Y. Lee, Y. C. Kang, *Chem. Eur. J.* **2016**, *22*, 2769 – 2774.
[76] G. D. Park, J. S. Cho, Y. C. Kang, *Nanoscale* **2015**, *7*, 16781 – 16788.
[77] J. H. Kim, Y. C. Kang, *Nano Res.* **2017**, *10*, 3178 – 3188.
[78] J. S. Cho, J. M. Won, J.-K. Lee, Y. C. Kang, *Nano Energy* **2016**, *26*, 466 – 478.
[79] J.-S. Park, Y. C. Kang, *J. Mater. Chem. A* **2017**, *5*, 8616 – 8623.
[80] J. K. Kim, S.-K. Park, J.-S. Park, Y. C. Kang, *J. Mater. Chem. A* **2019**, *7*, 2636 – 2645.
[81] G. D. Park, Y. C. Kang, *Chem. Eur. J.* **2016**, *22*, 4140 – 4146.
[82] G. D. Park, J.-H. Lee, Y. C. Kang, *Nanoscale* **2016**, *8*, 11889 – 11896.
[83] G. D. Park, J. H. Kim, Y. C. Kang, *Mater. Charact.* **2016**, *120*, 349 – 356.
[84] Y. N. Ko, S. Choi, S. Park, Y. Kang, *Nanoscale* **2014**, *6*, 10511 – 10515.
[85] Y. N. Ko, S. H. Choi, Y. C. Kang, *ACS Appl. Mater. Interfaces* **2016**, *8*, 6449 – 6456.
[86] S. H. Choi, Y. C. Kang, *Nanoscale* **2016**, *8*, 4209 – 4216.
[87] J. S. Cho, S.-K. Park, K. M. Jeon, Y. Piao, Y. C. Kang, *Appl. Surf. Sci.* **2018**, *459*, 309 – 317.
[88] G. D. Park, J. H. Kim, S.-K. Park, Y. C. Kang, *ACS Appl. Mater. Interfaces* **2017**, *9*, 10673 – 10683.
[89] S.-K. Park, Y. C. Kang, *ACS Appl. Mater. Interfaces* **2018**, *10*, 17203 – 17213.
[90] J. K. Kim, J. H. Kim, Y. C. Kang, *Chem. Eng. J.* **2018**, *333*, 665 – 677.
[91] J. H. Choi, S. K. Park, Y. C. Kang, *Small* **2019**, *15*, 1803043.
[92] J.-U. Seo, C.-M. Park, *J. Mater. Chem. A* **2014**, *2*, 20075 – 20082.
[93] K.-H. Nam, C.-M. Park, *J. Mater. Chem. A* **2016**, *4*, 8562 – 8565.
[94] D. A. Grishanov, A. A. Mikhaylov, A. G. Medvedev, J. Gun, P. V. Prikhodchenko, Z. J. Xu, A. Nagasubramanian, M. Srinivasan, O. Lev, *Energy Technol.* **2018**, *6*, 127 – 133.
[95] J. S. Cho, S. Y. Lee, J.-K. Lee, Y. C. Kang, *ACS Appl. Mater. Interfaces* **2016**, *8*, 21343 – 21349.
[96] A.-R. Park, C.-M. Park, *ACS Nano* **2017**, *11*, 6074 – 6084.
[97] K.-H. Nam, J.-H. Choi, C.-M. Park, *J. Electrochem. Soc.* **2017**, *164*, A2056 – A2064.
[98] G. Zhang, K. Liu, J. Zhou, *J. Mater. Chem. A* **2018**, *6*, 6335 – 6343.
[99] H. Yu, J. Yang, H. Geng, C. C. Li, *Nanotechnology* **2017**, *28*, 145403.
[100] J. S. Cho, H. S. Ju, J.-K. Lee, Y. C. Kang, *Nanoscale* **2017**, *9*, 1942 – 1950.

Manuscript received: June 1, 2019
Accepted manuscript online: July 21, 2019
Version of record online: August 23, 2019